Proposal of Novel Line-Start Type Self-Excited Wound-Field Synchronous Motor With Three-Phase Concentrated Winding Stator

IEEE Open Journal of
Industry Applications

Received 29 August 2020; revised 19 October 2020; accepted 3 November 2020. Date of publication 16 November 2020;
date of current version 3 December 2020.

Digital Object Identifier 10.1109/OJIA.2020.3036678

Proposal of Novel Line-Start Type Self-Excited Wound-Field Synchronous Motor With Three-Phase Concentrated Winding Stator

MASAHIRO AOYAMA [1] (Member, IEEE), MITSURU SAITO [1,2], TAKAHIRO MIZUTA [3], YOSHIHIRO MIYAMA [3,4] (Member, IEEE), AND KAZUMASA ITO [3]

[1] Shizuoka University, Hamamatsu 432-8561, Japan
[2] Nagoya Institute of Technology, Nagoya 466-8555, Japan
[3] Advanced Technology R&D Center, Mitsubishi Electric Corporation, Amagasaki 661-8661, Japan
[4] Himeji Works, Mitsubishi Electric Corporation, Himeji 670-0993, Japan

CORRESPONDING AUTHOR: MASAHIRO AOYAMA (e-mail: aoyama.masahiro@shizuoka.ac.jp)

ABSTRACT This paper describes a novel line-start type self-excited wound-field synchronous motor with three-phase concentrated winding stator. The unique feature of this proposed motor is that it accelerates by obtaining the induction torque from the slip frequency at the time of starting, and at the time of synchronous pull-in, it is driven synchronously with the second order space harmonic as the field magnetization power. First, the operation principle and the magnetic circuit design topologies will be described. Then, the prototype for principle verification and experimental setup will be revealed. Next, the result of evaluating the no-load synchronization pull-in characteristics in actual machine evaluation is reported.

INDEX TERMS Concentrated winding stator, line-start, self-excitation, synchronization, wound-field.

I. INTRODUCTION

As an industrial general-purpose motor that uses a fan or a pump as a load, a line-start type induction machine (IM) from a commercial AC power source has been widely used because of the demand for system cost reduction. Since the IM is a drive system that does not require an inverter or a rotor position sensor, it is low cost. But it requires an exciting current to obtain a field magnetic flux, which makes it difficult to achieve higher efficiency. As a research trend of improving the efficiency of IM, it has been reported that the resistance of the secondary conductor bar is reduced by adding silver, or copper is used instead of aluminum, and it is actually being introduced to the market [1], [2]. Since the resistance of the secondary conductor bar decreases, the maximum torque can be achieved with low slip, so that high power factor drive and secondary copper loss can be reduced [3], [4]. On the other hand, high efficiency can be achieved by adopting a permanent magnet type synchronous motor (PMSM) that does not require an exciting current for IM. However, since PMSM cannot be self-started in principle and requires an inverter and a magnetic pole position sensor, it has not been widely used in industrial general-purpose systems from the viewpoint of system cost. Therefore, research and development on a line-start PMSM (LS-PMSM) that adds a self-starting function by providing a secondary conductor on the outer circumference of the rotor is progressing. It is actually being put on the market [5]–[19]. In addition, recently, studies on the axial gap structure have been carried out for the purpose of improving the torque density of LS-PMSM [20]. This type of motor has a large output and high efficiency when synchronized. However, the brake torque is generated due to a permanent magnet magnetic flux which deteriorates the starting characteristics while asynchronous driving. In addition, there is a problem of demagnetization risk. This is because the harmonic flux of the slip frequency component interlinks with the permanent magnet at the time of asynchronous, and the eddy current is generated in the magnet to generate heat. Furthermore, LS-PMSM has a problem that it is difficult to reduce armature copper loss because it has a distributed winding stator structure. As another research with a different magnetic circuit topology, the first one is a brushless wound-field type three-phase synchronous motor that self-starts by using the Gerges

phenomenon at the time of starting [21]. This motor has a structural limitation such as a starter winding built into the stator and a switch for switching between the starter winding and the armature winding is required. The second one is a line-start type synchronous reluctance motor (LS-SynRM) in which a secondary conductor is embedded in a multi-layer flux barrier [22]–[26]. Since the torque can be generated by the synchronous reluctance torque during synchronization, the secondary copper loss can be reduced under synchronization. However, as with IM, there is no field source on the rotor side, so exciting current is required to obtain the field flux. Since most of them have distributed winding stator structure, it is difficult to reduce armature copper loss.

In view of the above problems, the authors are researching on the development of a new motor that can achieve higher performance than IM based on a concentrated winding stator structure. Since the concentrated winding structure can shorten the total coil length, it is possible to realize miniaturization and reduction of armature copper loss. In LS-PMSM, an expensive magnet with high coercive force is embedded in the rotor, but in the proposed motor, an electromagnet plays its role. As a feature different from the general separately excited wound-field type, it is a self-excited type in which a rectifier circuit is configured on the rotor using only passive elements. This paper proposes a line-start type self-excited wound-field synchronous motor (LS-SEWFM) based on a new operation principle, explains the magnetic circuit topology, and reports the evaluation results of the no-load synchronous pull-in characteristics with prototype.

II. MOTOR DESIGN

A. MACHINE DESIGN

Figure 1 shows the radial cross-sectional view of new line-start type self-excited wound-field synchronous motor. A rotor with a forward salient pole structure (0.35 mm thickness laminated steel sheet) is wound with two types of rotor windings, and an auxiliary pole (0.35 mm thickness laminated steel sheet) is placed between salient poles to form a magnetic circuit. 40 secondary conductor bars (A2017 material in JIS standard) are arranged on the outer diameter side of the rotor. The secondary conductor bars are short-circuited at a pitch of the number of poles as shown in Fig. 1(c), and each of the two short-circuited secondary conductor bars is independent from the other pairs. The two types of rotor windings are composed of an induction coil (I-coil) that obtains electromotive force from the 2nd space harmonic, and a field coil (F-coil) that forms a field pole through a diode. The rotor winding circuit is shown in Fig. 1(d). With this configuration, at the time of starting, an induced current having a slip frequency flows through the secondary conductor bar to generate an induction torque and accelerate. After reaching the synchronous speed, a field pole is formed by the 2nd space harmonic and rotates at the synchronous speed. Since the experiment is conducted in the facilities of the university's laboratory, the design is downsized from the actual required specifications, and the

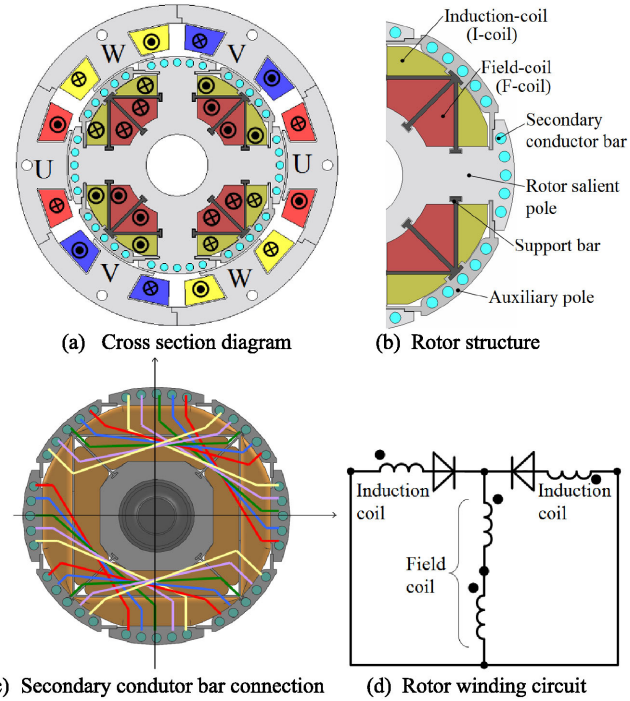

FIGURE 1. Proposed novel line-start machine.

TABLE 1 Main Specifications of Prototype

Parameter	Values
Stator outer diameter (mm)	125
Stack length (mm)	80
Air gap length (mm)	0.65
Rotor outer diameter (mm)	84.7
Armature winding connection	2-parrallel, Y-connection
Number of armature coil (turn/tooth)	100
Resistance of armature coil (Ω/coil)	0.84
Number of induction coil (turn/pole)	41
Number of field coil (turn/pole)	100
Resistance of induction coil (Ω/pole)	0.33 (average)
Resistance of field coil (Ω/pole)	0.86 (average)
Resistance of secondary conductor bar (mΩ/bar)	0.61

main specifications are as shown in Table 1. At present, the motor parameters are not optimized due to the initial principle verification stage. The difference between IM or LS-SynRM and LS-PMSM or LS-SEWFM depends on whether it is necessary to intentionally supply the excitation current from the armature side to obtain the field magnetic flux. In the proposed motor, the field magnetic flux is obtained from the armature magnetomotive force, but the space harmonics that were conventionally consumed as iron loss are utilized as the field flux source. From the next section, the magnetic circuit topology of the proposed motor will be explained.

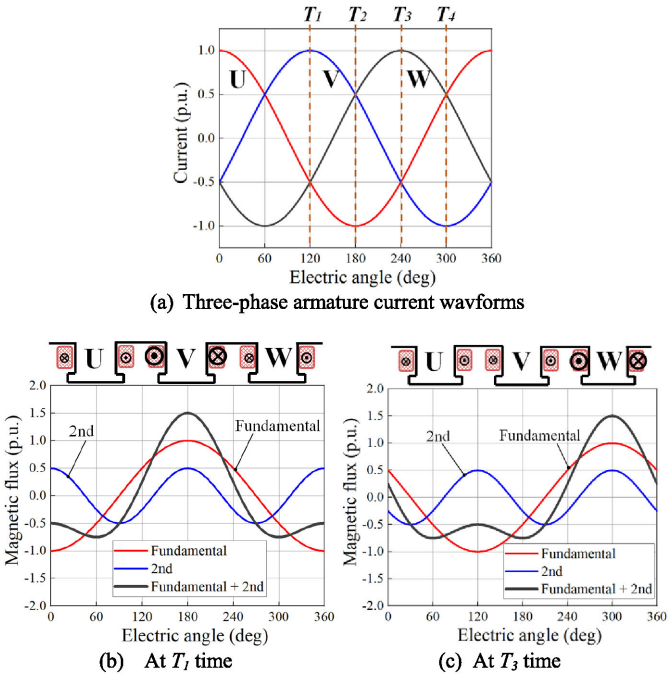

FIGURE 2. Three-phase armature waveforms and spatial magnetomotive force waveforms.

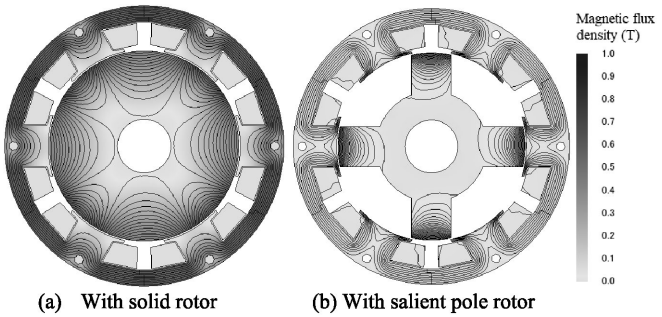

FIGURE 3. 2nd space harmonic distribution.

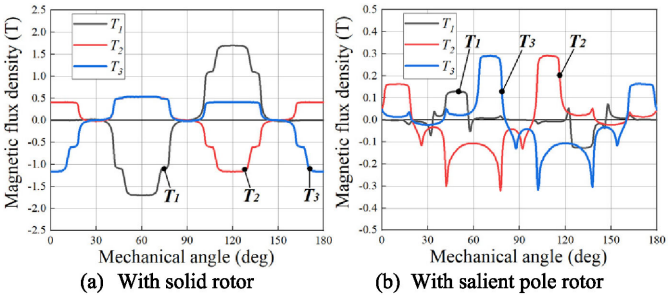

FIGURE 4. Air gap magnetic flux waveforms.

B. MAGNETIC CIRCUIT TOPOLOGY

As is well known, the gap magnetic flux waveform produced by the three-phase concentrated winding stator has the 2nd space harmonic superimposed in addition to the fundamental magnetic flux [27]. Figure 2(a) shows the three-phase sinusoidal current, and Fig. 2(b) and (c) shows the theoretical spatial distribution of the gap flux generated in the three-phase concentrated winding stator at the timing of T_1 and T_3 in Fig. 2(a). From this figure, the fundamental magnetic flux moves to the right, whereas the 2nd space harmonic moves to the left, and the 2nd space harmonic is in antiphase with the fundamental. When the above 2nd space harmonic is observed from the viewpoint of the rotor, in the case of a synchronous machine, the rotor rotates in the same direction as the fundamental waveform at the same frequency, and is therefore observed as a third time harmonic. From the above, in a general synchronous machine, iron loss occurs due to this harmonic magnetic flux. In PMSM, it also leads to the generation of magnet eddy current loss, so measures such as providing an appropriate flux barrier will be taken. On the other hand, for IM, in addition to slips on the fundamental waveform, electromotive force is generated in the secondary conductor due to slips on the harmonics. Therefore, the secondary current waveform is greatly distorted, which is a fact that deteriorates the performance. This is hindrance to improving the performance of the IM with three-phase concentrated winding stator. On the other hand, from a difference point of view, when the wound-field rotor is arranged in this three-phase concentrated winding stator, an induced electromotive force is generated by the 2nd space harmonic even when rotating at the synchronous speed. Based on this fact, in this research, based on a wound-field rotor, the induced electromotive force is obtained from the space harmonics generated in the three-phase concentrated winding stator. This electromotive force is used as the field source. Figure 3(a) shows the magnetic flux distribution of the 2nd space harmonic generated in a three-phase concentrated winding stator containing a circular rotor with no permeance distribution. The design constraint of the new general-purpose line-start type synchronous motor is 4 poles, so the rotor with 4 salient poles is included in the three-phase concentrated winding stator. Figure 3(b) shows the 2nd space harmonic flux distribution when the above salient pole rotor is included in a concentrated winding stator. Here, T_1, T_2 and T_3 in this figure are results of the gap magnetic flux waveform at the time of Fig. 2(a), respectively. Figure 4 shows the results of harmonic analysis of the gap magnetic flux waveform in Fig. 3. From this figure, the gap magnetic flux is modulated by the permeance distribution of the salient poles, so that the amplitude of the 2nd space harmonic becomes small. Mathematically expressing it, when a three-phase sinusoidal current (I_u, I_v and I_w) is given as shown in (1), the armature magnetomotive force F_s is given by (2).

$$\begin{cases} I_u = I_a \cos(\omega t - \delta) \\ I_v = I_a \cos\left(\omega t - \frac{2}{3}\pi - \delta\right) \\ I_w = I_a \cos\left(\omega t - \frac{4}{3}\pi - \delta\right) \end{cases} \tag{1}$$

Here, N is the number of turns of the armature coil, ω is the electrical angular velocity, and δ is the current phase, respectively. R_s means a spatial permeance distribution and is

given by (3).

$$F_s(t,\theta)=N\left\{I_u R_s(\theta)+I_v R_s\left(\theta-\frac{2}{3}\pi\right)+I_w R_s\left(\theta-\frac{4}{3}\pi\right)\right\} \tag{2}$$

$$R_s(\theta)=R_{s1}\cos\theta+R_{s2}\cos(2\theta-\pi) \tag{3}$$

Here, R_{s1} represents the fundamental wave component, R_{s2} represents the second harmonic component, θ is spatial rotor position, and the permeance distribution is approximated up to the 2nd order. Furthermore, based on the above results, the 2nd space harmonic has an opposite phase to the fundamental wave. By substituting (1) and (3) into (2) and rearranging, (4) can be obtained.

$$F_s(t,\theta)=\frac{3}{2}NI_a\left\{\begin{array}{c}R_{s1}\cos(\theta-\omega t+\delta)\\-R_{s2}\cos(2\theta+\omega t-\delta)\end{array}\right\}. \tag{4}$$

Here, when synchronized with $\theta=\omega$t, (4) can be summarized as (5).

$$F_s(t)=\frac{3}{2}NI_a\{R_{s1}\cos\delta-R_{s2}\cos(3\omega t-\delta)\} \tag{5}$$

Further, since the armature magnetomotive force (5) is magnetically modulated by the rotor salient pole permeance distribution $R_r(\theta)$ represented by (6), the gap magnetomotive force $F_{gap}(t)$ is represented by (7).

$$R_r(\theta)=R_{r0}+R_{r2}\cos(2\theta-\gamma) \tag{6}$$

$$F_{gap}(t)=\frac{3}{2}NI_a\left\{\begin{array}{l}R_{r0}R_{s1}\cos\delta-R_{r0}R_{s2}\cos(3\omega t-\delta)\\+R_{r2}R_{s1}\cos(2\omega t+\gamma)\\-\frac{1}{2}R_{r2}R_{s2}\cos(5\omega t-\delta+\gamma)\\-\frac{1}{2}R_{r2}R_{s2}\cos(\omega t-\delta-\gamma)\end{array}\right\} \tag{7}$$

Here, R_{r0} is the DC component of the rotor permeance distribution, R_{r2} is the permeance distribution generated by two salient poles per electrical angle cycle, γ is the phase of the permeance distribution, and $R_r(\theta)$ is approximated up to the second harmonic. For the sake of simplifying the mathematical expression, the approximation up to the 2nd space harmonic has been described, but as can be seen from the above, the salient pole permeance of the rotor reduces the amplitude of the 2nd space harmonic, and a new harmonic is generated. The concept of this research is the principle of obtaining an induced electromotive force from the 2nd space harmonic, so it is necessary to reduce the amplitude of other unnecessary harmonic orders while preventing the reduction of the amplitude of this harmonic. Therefore, as shown in Fig. 6, an auxiliary pole is arranged between the salient poles to improve the rotor permeance distribution in which R_{r2} is reduced while preventing the reduction of R_{r0} in (6). Figure 7 shows the air gap magnetic flux waveform and its harmonic analysis results in the magnetic circuit topology of Fig. 6. Comparing Fig. 5(b)and Fig. 7(b), it is possible to increase the 2nd space harmonic while preventing the reduction of the fundamental wave.

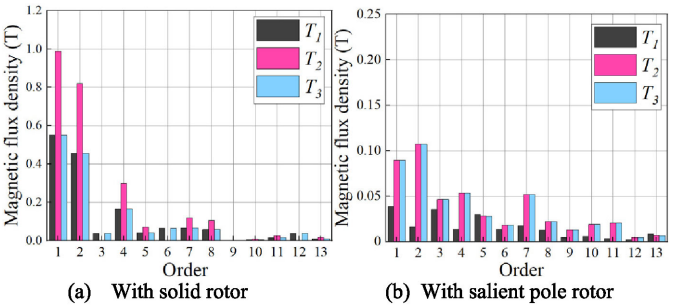

FIGURE 5. Harmonic contents of air gap magnetic flux waveforms.

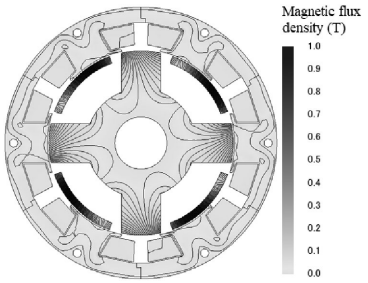

FIGURE 6. 2nd space harmonic distribution with salient pole rotor and auxiliary poles.

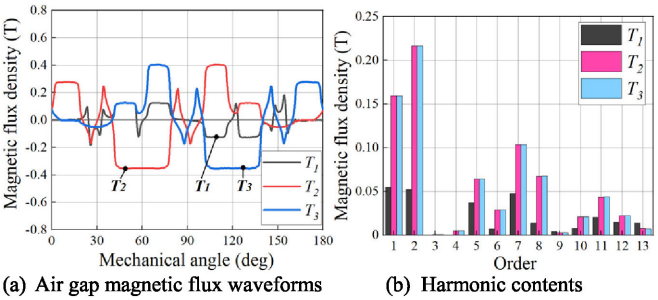

FIGURE 7. Air gap magnetic flux waveforms and its harmonic contents with salient pole rotor and auxiliary poles.

Next, the concept of the secondary conductor bar that generates an induction torque from the slip frequency for self-starting will be described. As stated in the concept, during synchronous drive, the induced electromotive force is obtained from the 2nd space harmonic and utilize as the field source. Therefore, during synchronization, it is desirable to eliminate magnetic interference so that the secondary current does not flow to the secondary conductor bar due to the 2nd space harmonic. However, in the case of a type which the secondary conductor bar is fully short-circuited with end ring by a general squirrel-cage type IM, secondary current is magnetically coupled with the 2nd space harmonic during synchronous driving. Therefore, as shown in Fig. 8, they are short-circuited and connected at the pole pitch of the fundamental wave, and the two secondary conductor pairs are connected independently from the other pairs. Therefore, in

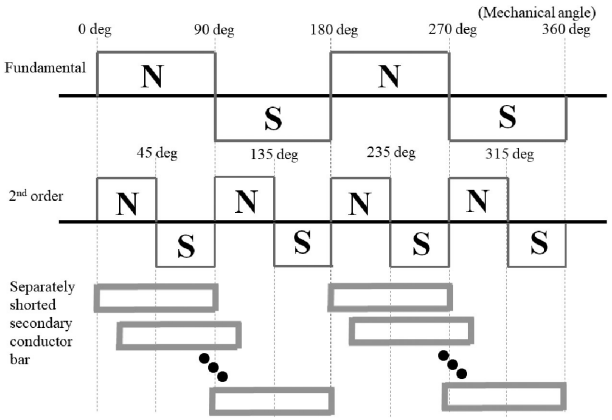

FIGURE 8. Separately shorted secondary conductor bar with pole-pitch.

the case of a 4-pole machine, the secondary conductor bars are short-circuited and connected at a 4-pole pitch.

C. FE SIMULATION

For electromagnetic field analysis, JMAG Designer ver. 18 from JSOL corp. was used. Analysis was performed with a sinusoidal voltage source using a two-dimensional cross-section model by the finite element method. The number of elements is 8990, the number of nodes is 5055, and the number of steps is 180 per period in electrical angle, respectively. First, the rotor winding connection will be examined by FE simulation. Immediately after direct start, the secondary conductor bar needs to obtain the induction torque form the slip frequency flux to accelerate. Then, the field poles need to be formed immediately after reaching the synchronous speed. The pulsation of the field flux at the field magnetic pole causes the increase in torque ripple and speed ripple. Since the proposed motor is wound-field motor based on the self-excitation principle, the field pole formation time is determined by the rotor winding inductance and rotor winding resistance. Furthermore, considering the mutual inductance, the armature winding inductance is also important design parameter. On the other hand, the number of turns of the armature winding is determined in order to obtain the required magnetomotive force. Therefore, the rotor inductance should be designed to be small. Figure 9 shows the rotor current waveform, armature current waveform, and magnetic flux waveform interlinking with the field coil due to the difference in the rotor winding connection under the same excitation condition. Here, "Condition-I" is a case where the rectifier circuit is configured by series connection, and "Condition-II" is connected for each pole pair. U1-coil is one of two U-phase armature windings connected in parallel. From this figure, it is predicted that when the rotor windings are connected in series, the field magnetic flux ripple increases, and the speed ripple increases. Therefore, it is desirable that the rotor winding is a one-pole par and is connected to the rotor winding rectifier circuit.

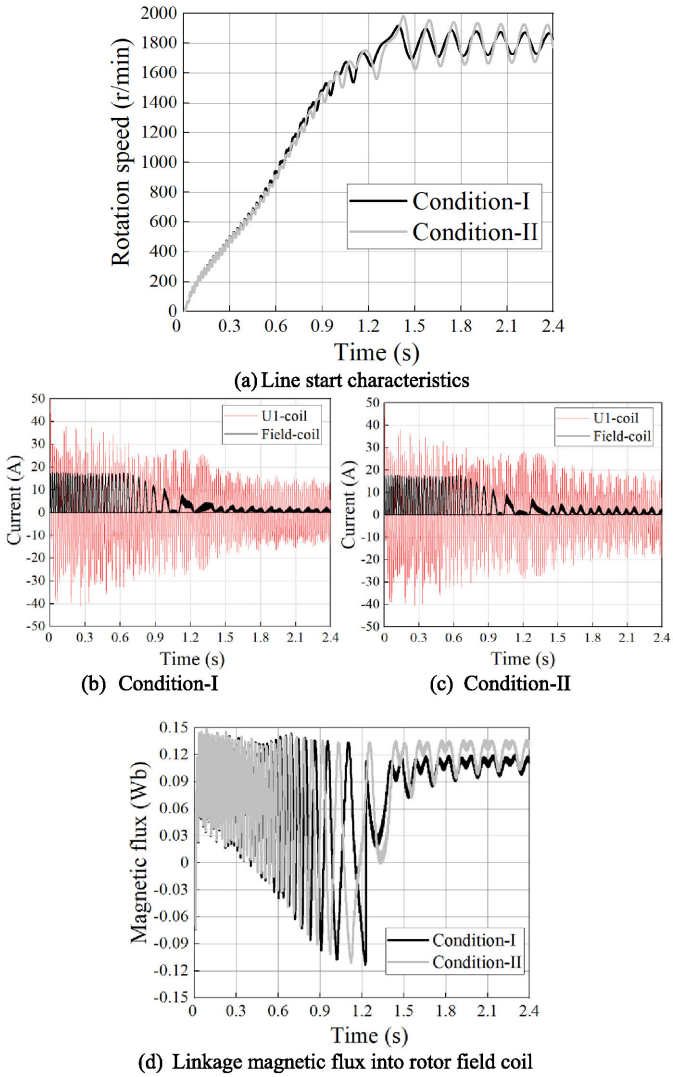

FIGURE 9. Line start characteristics compared with rotor coil connection pattern with applied voltage 70.7 V_{rms} under no-load.

Next, in order to clarify the characteristics at the time of asynchronous, the slip-*vs*.-torque characteristics were obtained by FE simulation. For reference, the results when the rotor winding is open and when the secondary conductor bar connection is open are shown for comparison. In FE simulation, when 100 V_{rms} is applied with 60 Hz three-phase sinusoidal voltage source, the rotor rotation speed is set to the constant speed at each speed. From this figure, it can be confirmed that the torque characteristic drops significantly just before the synchronous speed. That is, it is suggested that if the magnetomotive force is low, it may not be possible to pull in synchronously due to this drop in torque. During synchronous drive, two types of torque, reluctance torque and electromagnet torque, can be used, enabling high torque drive. Furthermore, Fig. 10 suggests interesting results. It can be self-started without the secondary conductor bar. This is thought to be due to the AC component of the field current

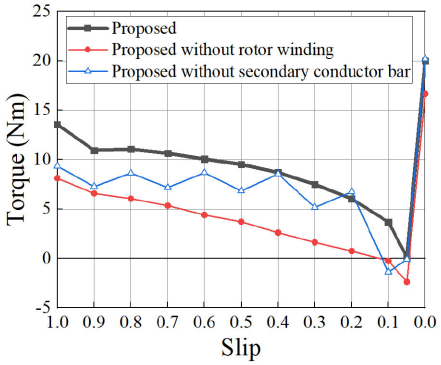

FIGURE 10. FE simulation results of slip-vs.-torque characteristics with applied voltage 100 V_{rms}.

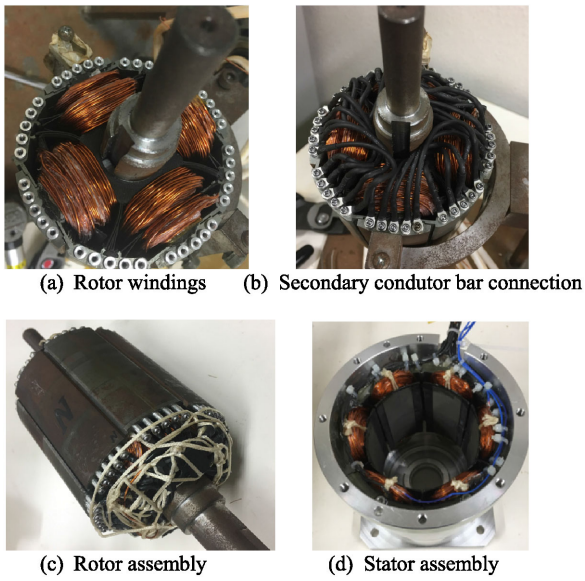

FIGURE 11. Actual prototype machine.

shown in Fig. 9, but it must be confirmed with the actual machine.

D. PROTOTYPE

Figure 11 shows the actual prototype. As the I-coil and F-coil, while removing the auxiliary poles, AIW copper wire with wire diameter ϕ 0.8 was wound around salient poles. Then, the auxiliary poles were attached, and the assembly was performed as shown in Fig. 11(a). From the viewpoint of assembling, the rotor core and the auxiliary poles are made of adhesively laminated electromagnetic steel sheets. The insulation between the rotor windings and the iron core is ensured by a 0.5 mm thick cover made by Markforged CFRP-3D printer. The space factor of the rotor winding is 21.5% for I-coil and 45.7% for F-coil due to the limitation of the coil end length of the rotor that can be housed in the motor housing and trial production by hand winding.

Next, the secondary conductor bar is connected as shown in Fig. 11(c). Here, the secondary conductor bar is machined into a cylindrical shape of ϕ3.1, and both ends are provided with taps for attaching M2 size screws in JIS standard. After inserting the secondary conductor bar into the hole for inserting the secondary conductor bar provided in the iron core, wire it using an AIW round wire with a wire diameter of ϕ1.1. Both ends of the secondary conductor bar were short-circuited with M2 screws with the round terminals as shown in Fig. 11(b). Here, since insulation treatment between the secondary conductor bar and the iron core is not performed, there is a concern that a cross current may occur, but detailed analysis and improvement in structural design will be a future work. Then, for the rotor winding, use the common cathode type SiC diode (ROHM SCS230AE2, $V_R = 650$ V, $I_F = 15$ A/leg) of the TO247 standard on the rotor with one pole pair to connect the rectifier circuit in Fig. 1(d). Then, as shown in Fig. 11(c), a rotor was prototyped by performing a racing process. To prevent centrifugal force, improve mechanical strength against electromagnetic force, and strengthen insulation between the winding and the iron core, resin (ThreeBond TB2022E) was used to fix the rotor winding and the circuit on the rotor. For the stator a split core was used for the purpose of facilitating trial manufacture and improving the space factor, and an AIW round wire with a wire diameter of ϕ0.8 was manually wound through an insulating bobbin of 0.9 mm. As shown in Fig. 11(d), after being mounted on the stator housing with bolts, it was fixed resin similarly to the rotor to secure mechanical strength and insulation between the winding and the iron core.

III. EXPERIMENTAL TEST

In this chapter, in order to confirm the operation principle described in the previous chapter, it is experimentally verified whether or not the synchronous pull-in can be performed by line-start under no-load.

A. INERTIA MEASUREMENT

This prototype is a motor prototyped for verification of the principle and is not designed with the required specifications. Therefore, load tests and tests to verify the allowable amount of load inertia will be demonstrated in the next development stage as the future works. However, it is important to grasp the inertia of the prototype itself, as represented by the motion equation (8), when performing synchronous pull-in under no-load. Therefore, as shown in Fig. 12(a), inertia measurement is performed by the two-point suspension method.

$$T_m - T_L - \mu_s r F_c = J \frac{\mathrm{d}^2\theta}{\mathrm{dt}^2} \tag{8}$$

$$T_m = T_{IM} - T_{field} \tag{9}$$

Here, T_m is the motor torque, T_L is the load torque, μ_s is the coefficient of static friction, r is the radius to the point of application of force, F_c is the normal force, J is the inertia,

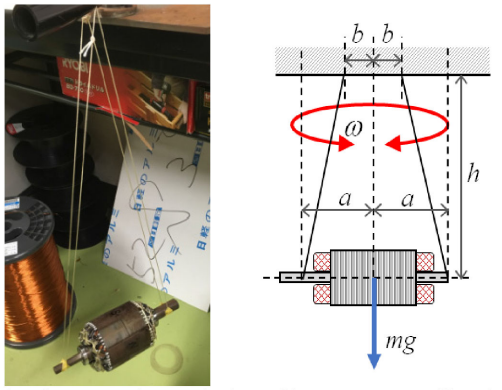

(a) 2-point suspension method (b) Measurment of inertia

FIGURE 12. Experimental test of measurement of inertia.

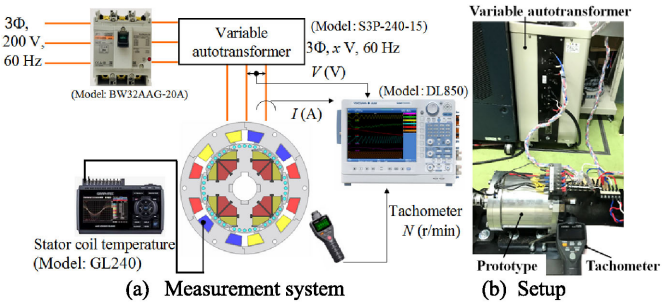

(a) Measurement system (b) Setup

FIGURE 13. Experimental setup.

and θ is the rotation angle. As shown in (9), T_m during non-synchronization is difference between the induction torque T_{IM} generated by the slip frequency and the braking torque T_{field} due to the field pole formed by the DC component of the field current. On the other hand, T_m under the synchronization is the sum of the reluctance torque T_{rel} and the self-excited electromagnet torque $T_{e\text{-}coil}$. The second term on the left side of (8) is added when a load is attached to the output shaft, and $T_L = 0$ when there is no load. After measuring the rotor mass with a weight scale and determining the center of gravity from the balance, the inertia J was measured by the above method. First, the parameters (a, b, mg, h) of Fig. 12(b) are measured from the arrangement of Fig. 12(a). Next, the string is twisted and vibrated. Then, the torsional vibration time T_b before stopping is measured. Using the torsional vibration frequency f calculated from T_b, the inertia J is calculated by the (11). As a result of the calculation, $J = 0.013198$ kgm^2.

$$J = \frac{mgab}{\omega^2 h} = \frac{mgab}{4\pi^2 f^2 h} \tag{10}$$

B. EXPERIMENTAL SETUP

Figure 13 shows the experimental environment setup. The prototype is driven by a commercial AC power supply while varying the voltage with a transformer via an electromagnetic breaker. When the rotation speed is detected using a rotary encoder, the inertia of the encoder is added to the inertia of the rotor itself. In this principle verification stage, in order to exclude these influences, a tachometer (FT3406 manufactured by HIOKI) that can be measured in a non-contact manner is used to measure with an oscilloscope using the analog output function. At the same time, a line voltage V and a phase current I shown in Fig. 14 are measured using a differential probe (Yokogawa 700925) and a current probe (RIGOL RP1001C).

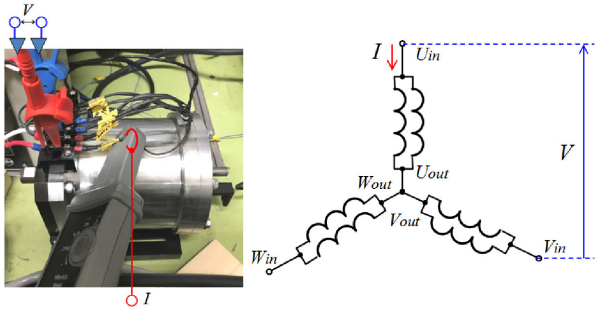

FIGURE 14. Measured point of line voltage and phase current.

C. SYNCHRONOUS PULL-IN EXPERIMENT UNDER NO-LOAD

Figure 15 shows the measurement results of line-start characteristics under no-load when the applied voltage V is 21.9 V_{rms}, 32.4 V_{rms}, 39.4 V_{rms}, 55.4 V_{rms}, 69.9 V_{rms}, 101.2 V_{rms}, 110.2 V_{rms} and 129.0 V_{rms}, respectively. In these figures, due to the limitation of the analog output function of the tachometer, the dead zone of the sensor is less than 300 r/min, and it is impossible to measure until it reaches 300 r/min. Due to the measurement principle of the tachometer, the rotation speed waveform during transition changes stepwise. In Fig. 15(a) to (e), if the line-start is performed in the state where the applied voltage is low, the magnetomotive force is insufficient and the synchronous pull-in cannot be performed, resulting in the IM drive mode. From (f) to (h) of Fig. 15, it can be confirmed that when driven with the enough applied voltage, the synchronous pull-in can be performed up to the synchronous speed (1800 r/min). For example, in the case of (f), it can be confirmed that the time from the line-start to the steady state in synchronization is 0.33 s, and in the case of (g) it reaches 0.3 s.

D. NO-LOAD LOSS

Figure 16(a) shows the line voltage and phase current during steady-state characteristics at the applied voltage 110.2 V_{rms}. In this experiment, a transformer is used to insulate the commercial power supply side from the load side as shown in Fig. 13, and the power source impedance is significantly increased. Therefore, the voltage waveform is likely to be distorted due to the voltage drop of the power source impedance even with a low load current as compared with the case where no transformer is used. For the above reason, the voltage waveform is distorted at the timing when the load current becomes maximum in Fig. 16(a). The no-load loss W_{noload}

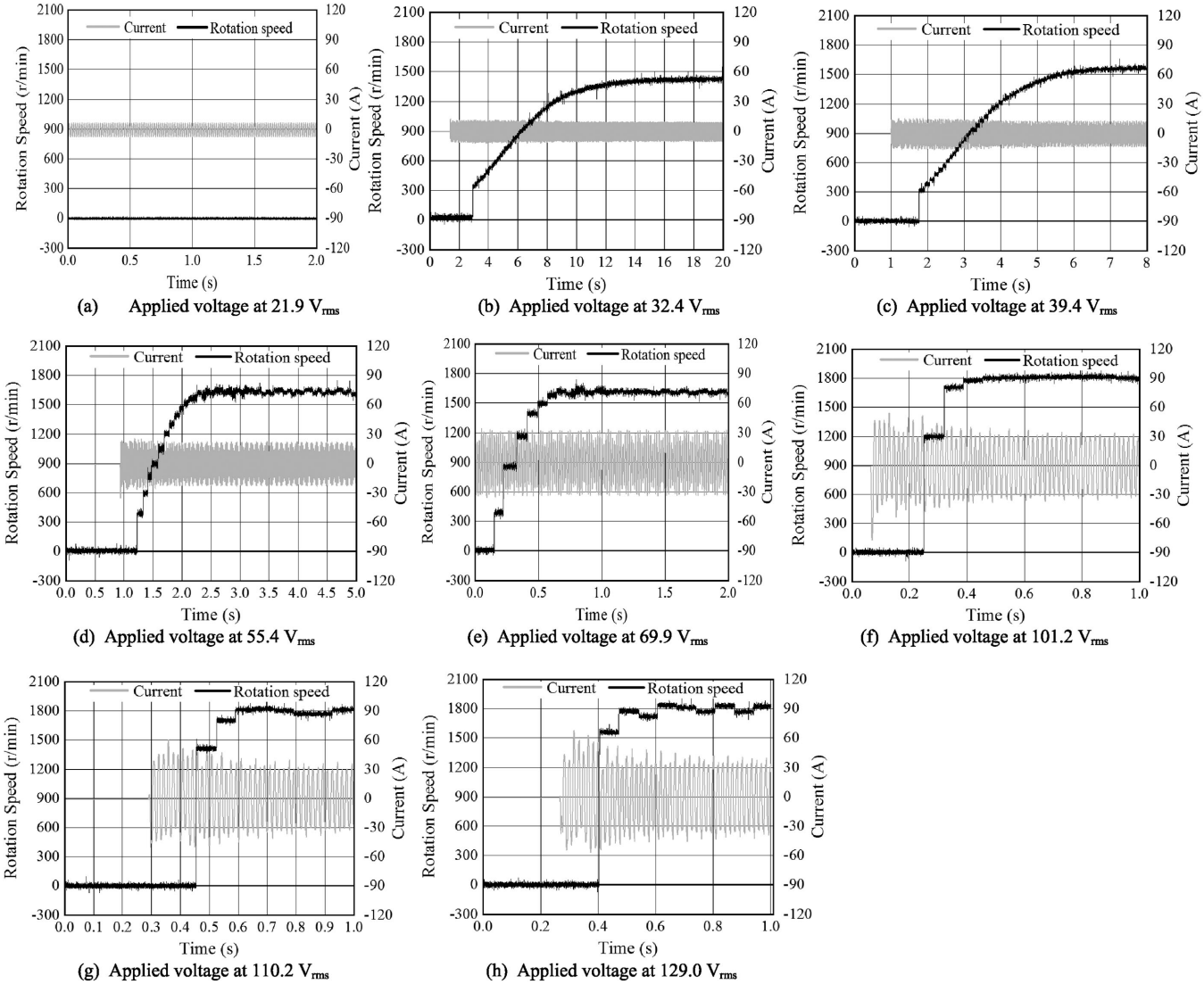

FIGURE 15. Line start characteristics with respect to applied voltage.

was obtained according to (11) to (16) using the results of harmonic analysis as shown in Figs. 16 (b) and (c).

$$S = V_p I = 1621.8\text{VA}, \tag{11}$$

$$Q = V_p I \sin\theta = 1542.8\text{var}, \tag{12}$$

$$P = V_p I \cos\theta = 500.2\text{W}, \tag{13}$$

$$P_{in} = 3P = 1500.6\text{W}, \tag{14}$$

$$W_{copper} = 3R_s I^2 = 818.0\text{W}, \tag{15}$$

$$W_{noload} = W_{iron} + W_{mecha} = P_{in} - W_{copper} = 682.2\text{W}. \tag{16}$$

Here, S is the apparent power per phase, Q is the reactive power per phase, P is the active power per phase, P_{in} is the input power, V_p is the phase voltage effective value, I is the phase current effective value, θ is the phase difference between voltage and current, R_s is the armature winding resistance, W_{copper} is the armature copper loss, and W_{mecha} is the no-load mechanical loss, respectively. Here, in the phase current waveform of Fig. 16(a), even-order harmonic superposition is observed, and the waveform is observed to be different for each period. The FFT analysis result in Fig. 16(c) is based on the waveform in the third period in Fig. 16(a). The line-start motor is open-loop driven without rotation speed control or current control. Therefore, speed ripple occurs due to torque ripple. As a result, pulsation occurs in the current waveform according to the change in torque value with respect to the rotation speed. That is, even-order harmonic is superimposed on the armature current or the amplitude is pulsating due to the speed ripple. The above numerical values are calculated using the values in the third period of Fig. 16(a). As a note, the conduction loss of the diode, the copper loss generated in the rotor winding, and the secondary copper loss in the secondary conductor bar are included in W_{iron} because it is

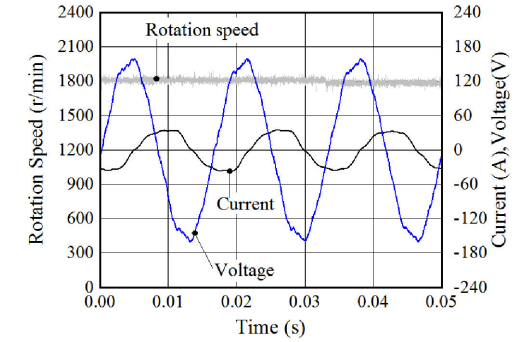

(a) Line voltage and phase current waveforms at 110.2 V_{rms}

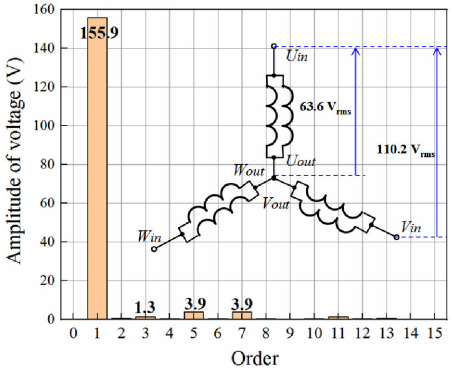

(b) Harmonic contents of line voltage at 110.2 V_{rms}

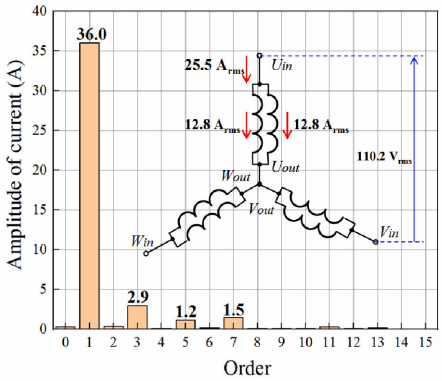

(c) Harmonic contents of phase current at 110.2 V_{rms}

FIGURE 16. Stationary characteristics with applied voltage at 110.2 V_{rms}.

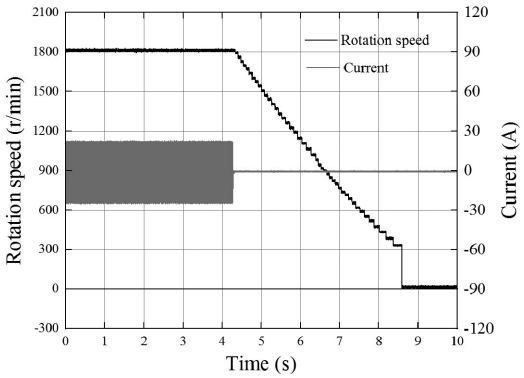

FIGURE 17. Coasting characteristics under no-load.

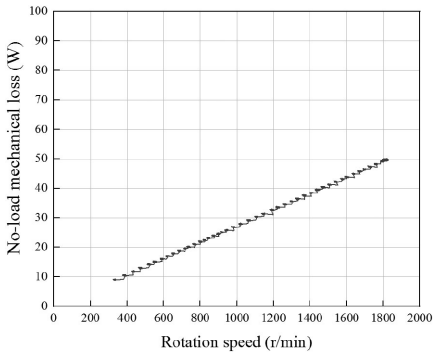

FIGURE 18. Mechanical loss under no-load.

difficult to measure. The no-load loss W_{noload} was calculated similarly for other applied voltages. Since the motor parameters such as the winding inductance have not been optimized for line-start type motor, the phase current value without load is excessively large. In the future, it is necessary to clarify the design guideline of the proposed motor.

In order to separate the no-load loss W_{noload} into the mechanical loss (including windage loss) W_{mecha} and the no-load iron loss W_{iron}, this section measures the mechanical loss by the coasting method. When the proposed motor is not supplied electric power, the 2nd space harmonic does not occur and no electromagnetic force is formed, so there is no loss due to field magnetic flux. Therefore, the experiment in which the power supply is stopped from the steady state after the synchronous pull-in and the inertial rotation is performed. The no-load loss when power is not supplied converts the rotational energy of the electric motor into heat energy, and the rotation speed gradually decreases. When the no-load loss W_{open}, the angular velocity ω, the torque τ generated by the no-load loss during no power supply, and the inertia J are used, W_{open} and τ are expressed by (17) and (18).

$$W_{open} = W_{mecha} = \omega\tau, \tag{17}$$

$$\tau = J\frac{\mathrm{d}\omega}{\mathrm{dt}}. \tag{18}$$

Figure 17 shows the coasting characteristics under no-load, and Fig. 18 shows the mechanical loss under no-load obtained by the coasting method. Figure 19 shows the result of obtaining the no-load iron loss W_{iron} by (16) from the mechanical loss W_{mecha} and the no-load loss W_{noload}. From this figure, the no-load loss increases as the applied voltage increases. In particular, for the no-load iron loss W_{iron}, the applied voltage is 101.2 V_{rms}, 110.2 V_{rms}, and 129.0 V_{rms}, all three conditions rotate at the synchronous speed, but the value of the no-load iron loss W_{rion} is significantly different. The 2nd space harmonic, which is energy source of the field flux, tend to increase passively as the armature current increases. Therefore, it is predicted that the no-load iron loss due to the field flux obtained by self-excitation will tend to increase. But

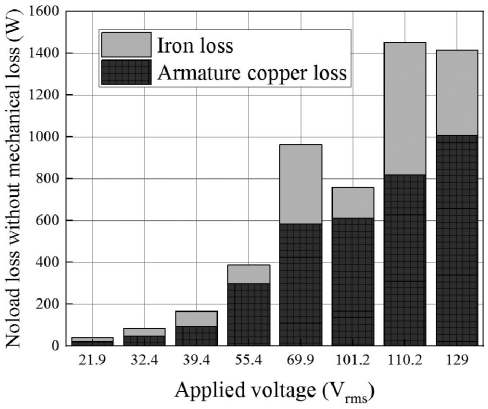

FIGURE 19. No-load loss without mechanical loss.

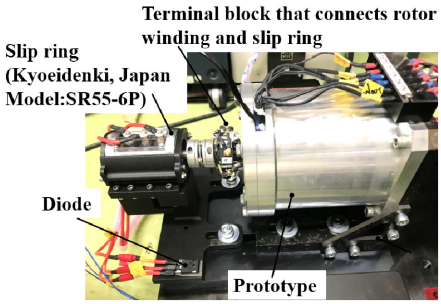

FIGURE 20. Prototype modified for rotor current measurement.

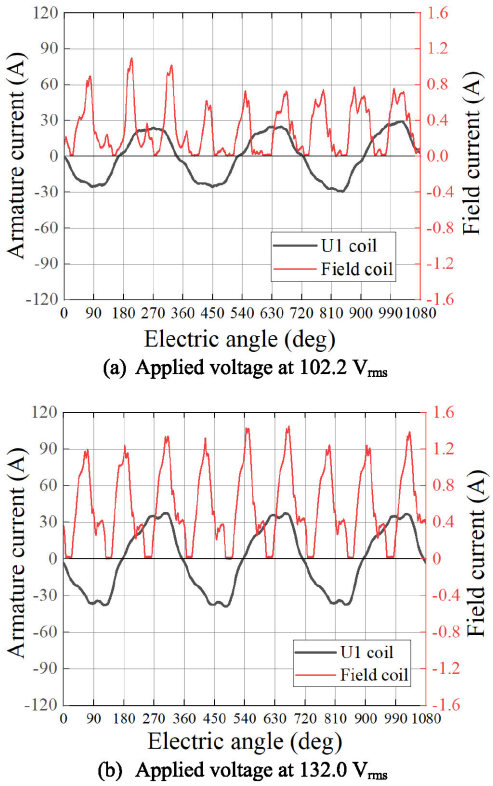

FIGURE 21. Measured U-phase armature current and self-excited rotor field current via slip ring under no-load.

this tendency is different under the above voltage conditions. In order to consider the cause of this, it is necessary to confirm how the rotor current changes at the timing of synchronous and asynchronous switching. In the next section, the prototype will be modified to measure the rotor current via the slip ring.

E. FIELD CURRENT MEASUREMENT

The field current is measured in this section in order to consider the fact that the field pole is formed by self-excitation and the effect of the field current on the speed ripple. Figure 20 shows experimental system in which the prototype of Fig. 12 was modified so that the rotor current could be measured via a slip ring. Here, as a precaution, the brush contact resistance and the rotor winding length have been changed by making the system capable of measuring the rotor current. As a result, the rotor winding resistance value is changing. Therefore, the rotor current and time constant change, which does not completely match the results up to the previous section. Figure 21 shows the phase current and field current waveforms after synchronous pull-in with no-load. From this figure, it can be confirmed that the amplitude of the field current increases because the armature magnetomotive force increases as the applied voltage increases. This is because when the armature current increases, the 2nd space harmonic passively increases, and the amount of harmonic flux interlinking with the rotor winding increases. On the other hand, it can be confirmed that the field current contains not only DC component but also the AC component. Furthermore, this AC component increases as the applied voltage increases. Since the field flux fluctuates due to the pulsation of the field current, it is considered that the speed ripple is observed in Figs. 15 (g) and (h). In the future, it will be necessary to improve the environment for measuring the rotation speed with a high-precision sampling frequency. It makes possible to analyze the relationship between the rotation speed ripple and field current ripple.

Next, an experiment is demonstrated on the effect of this field current ripple on the starting characteristics. First, open all the connections of the secondary conductor bar so that the secondary conductor bar does not generate induction torque. Fig. 22 shows the results of measuring the rotation speed and armature current when self-starting with no-load. From this figure, it can be seen that if the applied voltage is sufficiently high, self-starting and synchronous pull-in can be performed by the AC component of the field current without induction torque by the secondary conductor bar. On the other hand, comparing Fig. 15(f) and Fig. 22(b), the armature current of the latter is higher than that of the former. It is necessary to verify the change in power factor and the effect on synchronous torque due to the secondary conductor bar in the future. In addition, in terms of loss, it is important to deeply consider the effect of the AC component of this field current.

The comparison of W_{copper} and W_{iron} shows that the proportion of W_{copper} is higher. From this result, it is necessary to

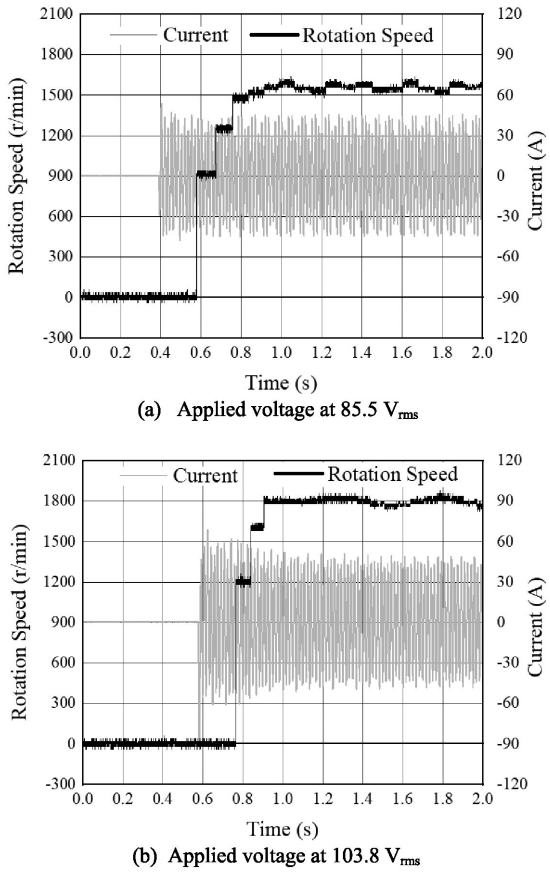

FIGURE 22. Line start characteristics with open secondary conductor bars.

optimize the motor parameters by examining the load test and evaluating the loss and clarifying the design guideline for this motor as the future works.

IV. CONCLUSION

In this paper, the new principle of self-starting synchronous motor was proposed for the purpose of line-start type industrial general-purpose motor applications. When the commercial AC power source is supplied, the secondary conductor bar accelerates by obtaining the starting torque from the slip frequency, and accelerates by the difference between the induction torque and the breaking torque caused by the DC component of the field current. As the further characteristic performance, the induction torque is also obtained by the AC component of the field current. During synchronization, it is driven as a self-excited wound-field synchronous motor with the 2nd space harmonic as the field source. These operations were verified experimentally.

Based on the knowledge obtained experimentally through this research, it is necessary to demonstrate load tests in the future to clarify the design guidelines for this motor. In addition, in order to analyze the causes of loss and clarify the design roadmap for improving efficiency, it is necessary to perform detailed loss separation under each drive condition based on the measurement result of the rotor current.

The final goal of this research is to develop a new line-start type synchronous motor that satisfies the IE4 efficiency standard with a general-purpose motor of several kW for industrial use.

REFERENCES

[1] A. T. de Almeida, F. J. T. E. Ferreira, and G. Baoming, "Beyond induction motors—Technology trends to move up efficiency," *IEEE Trans. Industry Appl.*, vol. 50, no. 3, pp. 2103–2114, May/Jun. 2014.

[2] F. J. T. E. Ferreira, B. Leprettre, and A. T. de Almeida, "Comparison of protection requirements in IE2-, IE3-, and IE4-class motors," *IEEE Trans. Industry Appl.*, vol. 52, no. 4, pp. 3603–3610, Jul./Aug. 2016.

[3] A. T. De Almeida, F. J. T. E. Ferreira, and A. Q. Duarte, "Technical and economical considerations on super high-efficiency three-phase motors," *IEEE Trans. Industry Appl.*, vol. 50, no. 2, pp. 1274–1285, Mar./Apr. 2014.

[4] X. Liang and O. Ilochonwu, "Induction motor starting in practical industrial applications," *IEEE Trans. Industry Appl.*, vol. 47, no. 1, pp. 271–280, Jan./Feb. 2011.

[5] A. M. Knight and C. I. McClay, "The design of high-efficiency line-start motors," *IEEE Trans. Industry Appl.*, vol. 36, no. 6, pp. 1555–1562, Nov./Dec. 2000.

[6] R. T. Ugale, B. N. Chaudhari, and A. Pramanik, "Overview of research evolution in the field of line start permanent magnet synchronous motors," *IET Electric Power Appl.*, vol. 8, no. 4, pp. 141–154, Apr. 2014.

[7] K. Kurihara and M. A. Rahman, "High-efficiency line-start interior permanent-magnet synchronous motors," *IEEE Trans. Industry Appl.*, vol. 40, no. 3, pp. 789–796, May/Jun. 2004.

[8] M. Lin, D. Li, Y. Zhao, X. Ren, and R. Qu, "Improvement of starting performance for line-start permanent magnet motors by winding reconfiguration," *IEEE Trans. Industry Appl.*, vol. 56, no. 3, pp. 2441–2450, May/Jun. 2020.

[9] E. Peralta-Sanchez and A. C. Smith, "Line-start permanent-magnet machines using a canned rotor," *IEEE Trans. Industry Appl.*, vol. 45, no. 3, pp. 903–910, May/Jun. 2009.

[10] B. Stumberger, T. Marcic, and M. Hadziselimovic, "Direct comparison of induction motor and line-start IPM synchronous motor characteristics for semi-hermetic compressor drives," *IEEE Trans. Industry Appl.*, vol. 48, no. 6, pp. 2310–2321, Nov./Dec. 2012.

[11] T. Marcic, B. Stumberger, and G. Stumberger, "Comparison of induction motor and line-start IPM synchronous motor performance in a variable-speed drive," *IEEE Trans. Industry Appl.*, vol. 48, no. 6, pp. 2341–2352, Nov./Dec. 2012.

[12] M. J. Melfi, S. D. Umans, and J. E. Atem, "Viability of highly efficient multi-horsepower line-start permanent-magnet motors," *IEEE Trans. Industry Appl.*, vol. 51, no. 1, pp. 120–128, Jan./Feb. 2015.

[13] A. J. Sorgdrager, R. Wang, and A. J. Grobler, "Multiobjective design of a line-start PM motor using the Taguchi method," *IEEE Trans. Industry Appl.*, vol. 54, no. 5, pp. 4167–4176, Sep./Oct. 2018.

[14] R. T. Ugale and B. N. Chaudhari, "Rotor configurations for improved starting and synchronous performance of line start permanent-magnet synchronous motor," *IEEE Trans. Ind. Electron.*, vol. 64, no. 1, pp. 138–148, Jan. 2017.

[15] S. F. Rabbi and M. A. Rahman, "Critical criteria for successful synchronization of line-start IPM motors," *IEEE J. Emerg. Sel. Top. Power Electron.*, vol. 2, no. 2, pp. 348–358, Jun. 2014.

[16] B. Yan, Y. Yang, and X. Wang, "Design of a large capacity line-start permanent magnet synchronous motor equipped with hybrid salient rotor," *IEEE Trans. Ind. Electron.*

[17] D. Mingardi and N. Bianchi, "Line-Start PM-Assisted synchronous motor design, optimization, and tests," *IEEE Trans. Ind. Electron.*, vol. 64, no. 12, pp. 9739–9747, Dec. 2017.

[18] D. Mingardi, N. Bianchi, and M. D. Prè, "Geometry of line start synchronous motors suitable for various pole combinations," *IEEE Trans. Industry Appl.*, vol. 53, no. 5, pp. 4360–4367, Sep./Oct. 2017.

[19] A. Waheed and J. Ro, "Analytical modeling for optimal rotor shape to design highly efficient line-start permanent magnet synchronous motor," *IEEE Access*, vol. 8, pp. 145672–145686, 2020.

[20] S. Kahourzade, A. Mahmoudi, R. Ravji, and W. L. Soog, "Line-Start axial-flux PM motors: Introduction of a new machine topology," in *Proc. IEEE Energy Convers. Congr. Expo.*, pp. 7027–7034.

[21] T. Fukami, R. Miyamoto, T. Miyamoto, and F. Shibata, "Self-starting, self-excited, brushless three-phase synchronous motor," T. IEE Japan, vol. 114-D, no. 4, pp. 470–471, 1994, in Japanese.
[22] A. Kersten, Y. Liu, D. Pehrman, and T. Thiringer, "Rotor design of line-start synchronous reluctance machine with round bars," *IEEE Trans. Industry Appl.*, vol. 55, no. 4, pp. 3685–3696, Jul./Aug. 2019.
[23] J. Tampio, T. Känsäkangas, S. Suuriniemi, J. Kolehmainen, L. Kettunen, and J. Ikäheimo, "Analysis of direct-on-line synchronous reluctance machine start-up using a magnetic field decomposition," *IEEE Trans. Industry Appl.*, vol. 53, no. 3, pp. 1852–1859, May/Jun. 2017.
[24] M. Gamba, E. Armando, G. Pellegrino, A. Vagati, B. Janjic, and J. Schaab, "Line-Start synchronous reluctance motors: Design guidelines and testing via active inertia emulation," in *Proc. IEEE Energy Convers. Congr. Expo.*, 2015, pp. 4820–4827.
[25] Y. Hu, B. Chen, Y. Xiao, J. Shi, and L. Li, "Study on the influence of design and optimization of rotor bars on parameters of a line-start synchronous reluctance motor," *IEEE Trans. Industry Appl.*, vol. 56, no. 2, pp. 1368–1376, Mar.-Apr. 2020.
[26] B. Poudel, E. Amiri, and P. Rastgoufard, "Design and analysis of line start synchronous reluctance motor with dual saliency," in *Proc. IEEE Transp. Electrific. Conf. Expo*, 2018, pp. 385–388.
[27] M. Aoyama and T. Noguchi, "Permanent-magnet-free-synchronous motor with self-excited wound-field technique utilizing space harmonics," in *Proc. IEEE Appl. Power Electron. Conf. Expo.*, 2017, pp. 3187–3194.

MASAHIRO AOYAMA (Member, IEEE) was born in Shizuoka, Japan in 1984. He received the B. Eng. degree in electric engineering from the Nagaoka University of Technology, Niigata, Japan in 2006, M. Eng. degree in advanced engineering course from Toyota Technical Institute, Nagoya, Japan in 2008, and the D. Eng. degree in engineering with the Department of Environment and Energy System, Shizuoka University, Shizuoka, Japan in 2015.

In 2008, he was with Suzuki Motor Corporation, Hamamatsu, Japan. After engaging in research on traction motors for electric vehicles, he retired in March 2018. Since April 2018, he has been an Assistant Professor with the Department of Electrical and Electronics Engineering, Shizuoka University, Hamamatsu, Japan. His research interests include electric machine design and its motor drives.

Dr. Aoyama is a member of the IEEE Industry Applications Society, Power and Energy Society, Industrial Electronics Society, and the Institute of Electrical Engineers of Japan.

MITSURU SAITO was born in Ibaraki, Japan in 1997. He received the B. Eng. degree in electrical and electronics engineering from Shizuoka University, Shizuoka, Japan in 2020. Since April 2020, he has been studying with Electrical and Mechanical Engineering Program, Nagoya Institute of Technology, Nagoya, Japan. His research interests include electric machine design and its motor drives. Mr. Saito is a Student Member of the Institute of Electrical Engineers of Japan.

TAKAHIRO MIZUTA was born in 1988. He received the M. Eng. degree with the Department of Applied Physics, School of Engineering, the University of Tokyo, Tokyo, Japan in 2013.

Since 2013, he has been with Advanced Technology R&D Center, Mitsubishi Electric Corporation, Hyogo, Japan, where he has been involved in research and development of electric machines.

Mr. Mizuta is a Member of the Institute of Electrical Engineers of Japan.

YOSHIHIRO MIYAMA (Member, IEEE) was born in 1983. He received the M. Eng. degree with the Department of Science and Engineering, Ritsumeikan University, Shiga, Japan in 2009, and the D. Eng. degree with the Graduate School of Functional Control Systems, Shibaura Institute of Technology, Tokyo, Japan in 2019.

In 2009, he was with Advanced Technology R&D Center, Mitsubishi Electric Corporation, Hyogo, Japan, where he was involved in research and development of high-performance motor and its drive systems. Since 2020, he has been with the Himeji Works, Mitsubishi Electric Corporation, Himeji, Japan, where he is developing traction motors for automotive applications.

Dr. Miyama is a Member of the IEE and the SAE of Japan.

KAZUMASA ITO was born in 1978. He graduated from Nagoya University, Aichi, Japan and received the M. Eng. degree in engineering in 2002. In April 2002, he was with Advanced Technology R&D Center, Mitsubishi Electric Corporation, Hyogo, Japan, where he was involved in research and development of electric machines. In 2010, he transferred to Nagoya Works, Mitsubishi Electric Corporation, Aichi, Japan, where he developed the servo amplifier for factory automation. Since April 2013, he has been with Advanced Technology R&D Center.

He was a Corporate Affiliate Visiting Fellow with the Walter H. Shorenstein Asia-Pacific Research Center (Shorenstein APARC), Stanford University, Stanford, USA for academia year of 2017 – 2018. His research interest includes high-performance electric motor and its drive systems.

Mr. Ito is a Member of the Institute of Electrical Engineers of Japan.